Arabian Journal of Chemistry 16 (2023) 105198

Contents lists available at ScienceDirect

Arabian Journal of Chemistry

journal homepage: www.sciencedirect.com

Original article

Effect of cellulose derivatives on the morphology, agglomeration, and phase transformation of spinel nanoparticles prepared via modified sol-gel method and comparison of optical transmission of spark plasma sintered ceramic

Fuqiu Ye [a,*], Mohsen Sadeghi [b], M.R. Loghman Estarki [b]

[a] Department of Physics, Jishou University, Jishou 416000, People's Republic of China
[b] Department of Materials Engineering, Malek Ashtar University of Technology, Iran

ARTICLE INFO

Article history:
Received 1 May 2023
Accepted 8 August 2023
Available online 14 August 2023

Keywords:
Transparent ceramic
Carboxymethyl cellulose
Sol–gel
Spark plasma sintering
HPMC

ABSTRACT

The Pechini method is one of the alkoxide sol–gel methods in which citric acid (CA) and ethylene glycol (EG) pair are used for gel preparation. The major downside of this method is an agglomeration of the produced nanoparticles. In this research, by substituting ethylene glycol chelating agent with cellulose derivatives (such as carboxy methyl cellulose (CMC) and hydroxy propyl methyl cellulose (HPMC), the reduction of the extent of spinel nanoparticle agglomeration is examined. To this aim, a different ratio of CMC and HPMC to metal ions (Mg^{2+} and Al^{3+}) was used. The results indicated that the sample synthesized with 1 g CMC had the minimum agglomeration and particle size (50 nm). Next, this sample was consolidated through the spark plasma sintering method at 1500 °C for 15 min. The microstructure, grain size and optical transmittance of the SPSed body were compared with the sample prepared with the conventional Pechni method. The results showed that the maximum visible light and infrared transmission of the bulk prepared from the modified Pechini method was higher than that of the sample prepared via the conventional Pechini method. The optimal visible light transmission was 85%, and in the IR region at a wavelength of 5 μm was 75%. This is related to the higher apparent density of this ceramic (99.98% vs 98.82%) and the lower porosity of this sample.

1. Introduction

The progressive advances in science and technology have intensified the need to use materials with superior properties. An issue that has attracted much attention is magnesium aluminate spinel ($MgAl_2O_4$). Optically, this ceramic offers good transmission in the visible light and infrared regions of the electromagnetic spectrum. Also, it has high mechanical hardness. Typically, transparent ceramics are obtained through the sintering of spinel nanoparticles (Senina et al., 2019; Izadbakhsh et al., 2021; Bykov et al., 2019; Azizi-Malekabadi et al., 2020; Baruah et al., 2023). There are various methods for preparing spinel nanoparticles, including mechanical alloy making, coprecipitation, hydrothermal synthesis method, plasma spraying degradation, sol–gel (alkoxide and non-alkoxide), as well as combustive sol–gel. Meanwhile, the Pechini sol–gel method has attracted much attention thanks to enjoying high homogeneity and uniformity, low synthesis temperature, high purity percentage, easy process control, non-toxicity, use of available and relatively inexpensive initial salts, as well as availability. The morphology and extent of agglomeration of the precursor play a key role in the synthesis of transparent ceramics (Nassar et al., 2014; Durai et al., 2022; Wen et al., 2017). The problem with the Pechini method is an agglomeration of produced nanoparticles (Medvedev et al., 2022; Mamonova et al., 2017).

CMC and HPMC as chelating agents were used for the synthesis of some metal oxides nanoparticles, such as iron oxide and $MnFe_2O_4$ nanoparticles (Sanjabi et al., 2015; Hasanpour et al., 2017;

* Corresponding authors.
E-mail addresses: phyfq@jsu.edu.cn (F. Ye), mrlestarki@mut-es.ac.ir (M.R. Loghman Estarki).
Peer review under responsibility of King Saud University.

Production and hosting by Elsevier

https://doi.org/10.1016/j.arabjc.2023.105198
1878-5352/

Table 1
The precursor used in this work.

No.	Powder name	Purity percentage	Company name	Country
1	Yttrium chloride	99.9	Merck	Germany
2	Aluminium chloride	99.9	Sigma Aldrich	Germany
3	Carboxymethyl cellulose	99.9	Sigma Aldrich	Germany
4	Anhydrous citric acid	99.9	Merck	Germany
5	Magnesium nitrate hexahydrate	99.9	Merck	Germany
6	hydroxy propyl methyl cellulose	99.9	Sigma Aldrich	Germany

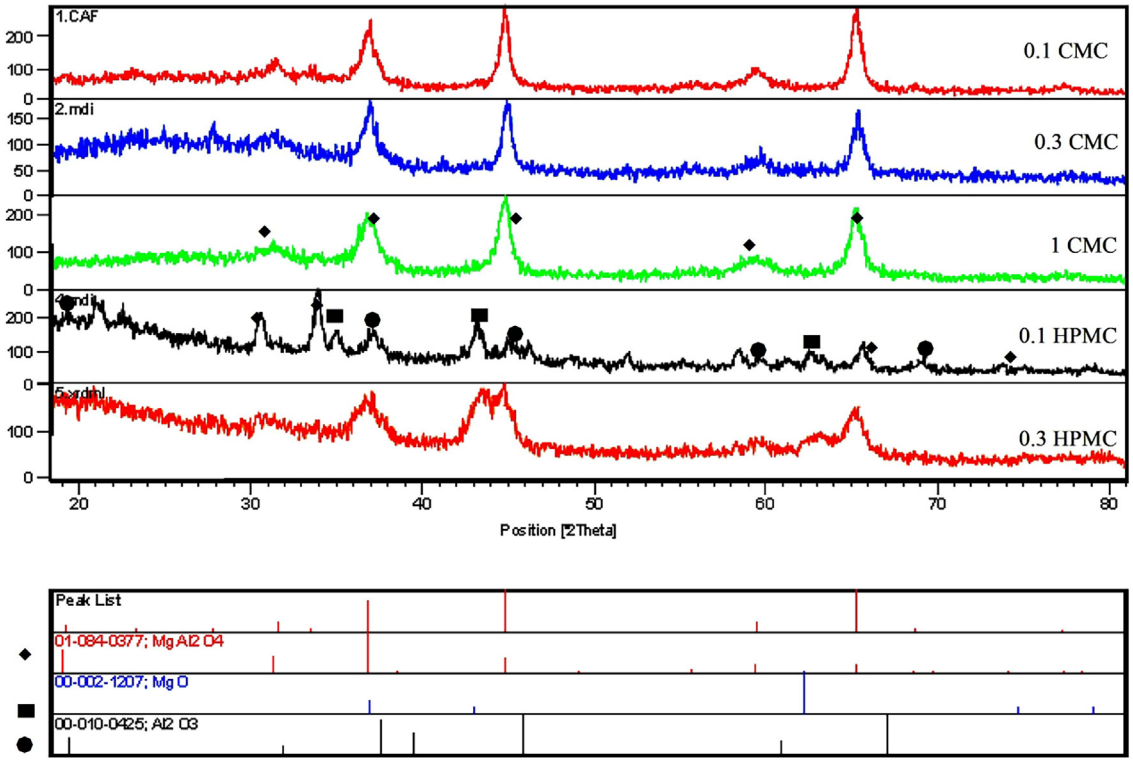

Fig. 1. XRD patterns of spinel nanoparticles synthesized via the modified Pechini method with varying amounts of CMC and HPMC content.

Akhlaghi et al., 2022; Gogoi et al., 2017). But, there are no reports on the synthesis of $MgAl_2O_4$ nanoparticles via CMC-citric acid pair. In this research, the effect of substituting ethylene glycol with CMC and HPMC agent is examined at different ratios on the shape, size of particles, and phase of spinel nanoparticles. Furthermore, to the best of our knowledge, there is no study to compare IR and visible transmittance of spinel ceramics fabricated with Pechni and modified Pechini methods.

Various sintering methods have been reported for the synthesis of homogeneous magnesium aluminate spinel ceramics, including pressureless sintering, hot isostatic pressing, spark plasma sintering, microwave sintering, etc. In addition, different materials, including Y_2O_3, B_2O_3, ZrO_2, LiF, etc., have been used as a sintering aid in the sintering process, and their results have been investigated (Senina et al., 2019; Rothman et al., 2014; Sutorik et al., 2012; Zhang et al., 2023). Among the stated sintering aids, yttria has offered good results in improving the densification of spinel ceramics (Zhang et al., 2023; Bykov et al., 2019).

In this project, to achieve magnesium aluminate spinel nanoparticles powder with a uniform size distribution and high purity, the wet chemistry method (Pechini method modified with CMC and HPMC is used), after identifying the samples in terms of morphology, elemental analysis and phase, the optimized nanopowder is chosen and then sintered via spark plasma sintering methods, so that a transparent spinel disc would form.

2. Experimental

2.1. Materials

The initial raw materials used included aluminium chloride and yttrium chloride sintering aid, whose purity percentage and manufacturer's company are presented in Table 1.

2.2. Synthesis of spinel nanoparticles via modified Pechini method

In this method, 6.7 g aluminium chloride, 3.6 g magnesium nitrate hexahydrate, and different amounts of carboxymethyl cellulose (0.1 (100 g/lit), 0.3 (300 g/lit), and 1.0 g (4 g/lit)) or 0.1 (100 g/lit) and 0.3 g (300 g/lit) hydroxy propyl methyl cellulose (HPMC) were mixed in 250 ml distilled water. Next, 7.54 g citric acid (equivalent to a 4 times mole ratio of aluminium and magnesium salt) was dissolved in 250 ml water and added dropwise to the previous solution. Eventually, the resulting solution was placed on a magnetic stirrer. The mixture of the reactants was exposed to 80 °C for 1 h. It was then exposed to 150 °C for 1 h for gel formation. The formed gel was exposed to 200 °C for 1 h to obtain the dry

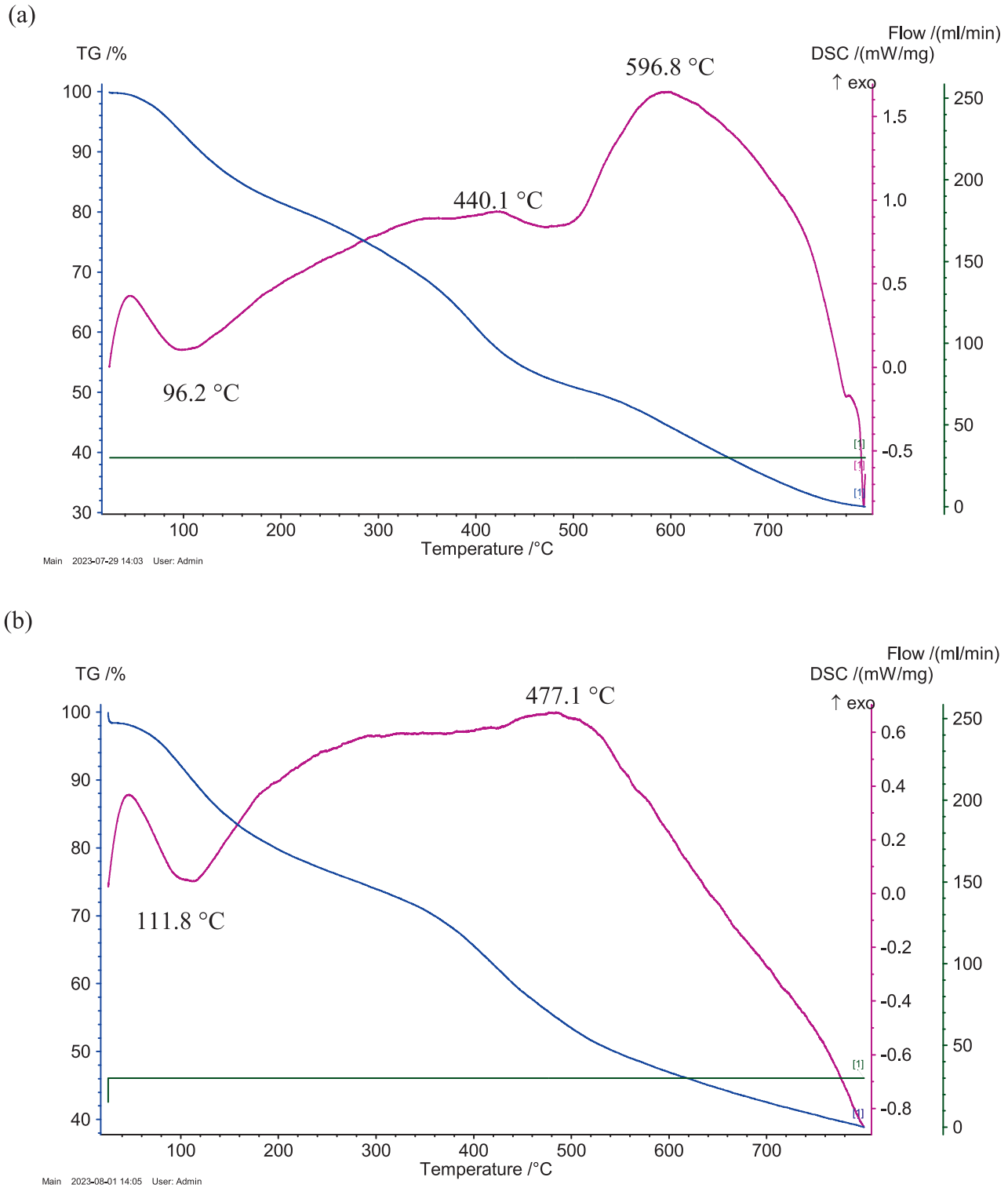

Fig. 2. TG/DSC analysis of spinel gel obtained from CMC (a) and HPMC (b) precursor.

gel. Thereafter, it was calcined at 800 °C for 2 h to obtain magnesium aluminate spinel nanoparticles.

2.3. Synthesis of spinel nanoparticles by conventional Pechini method

In this method, 6.7 g aluminium chloride, 3.6 g magnesium nitrate hexahydrate, and 10 ml ethylene glycol were mixed in 250 ml distilled water. Next, citric acid solution (7.54 g@250 ml water) was used with the amount of four times of Mg and Al ions added dropwise to the previous solution. Ultimately, the resulting solution was exposed to 80 °C/1h and 150 °C/1h to obtain the gel. Finally, the dry gel was calcined at 800 °C/2h to obtain the magnesium aluminate spinel nanoparticles. To reduce agglomaration degree, spinel nanoparticles were ball-milled with zirconia balls for 6h (Wang et al., 2023).

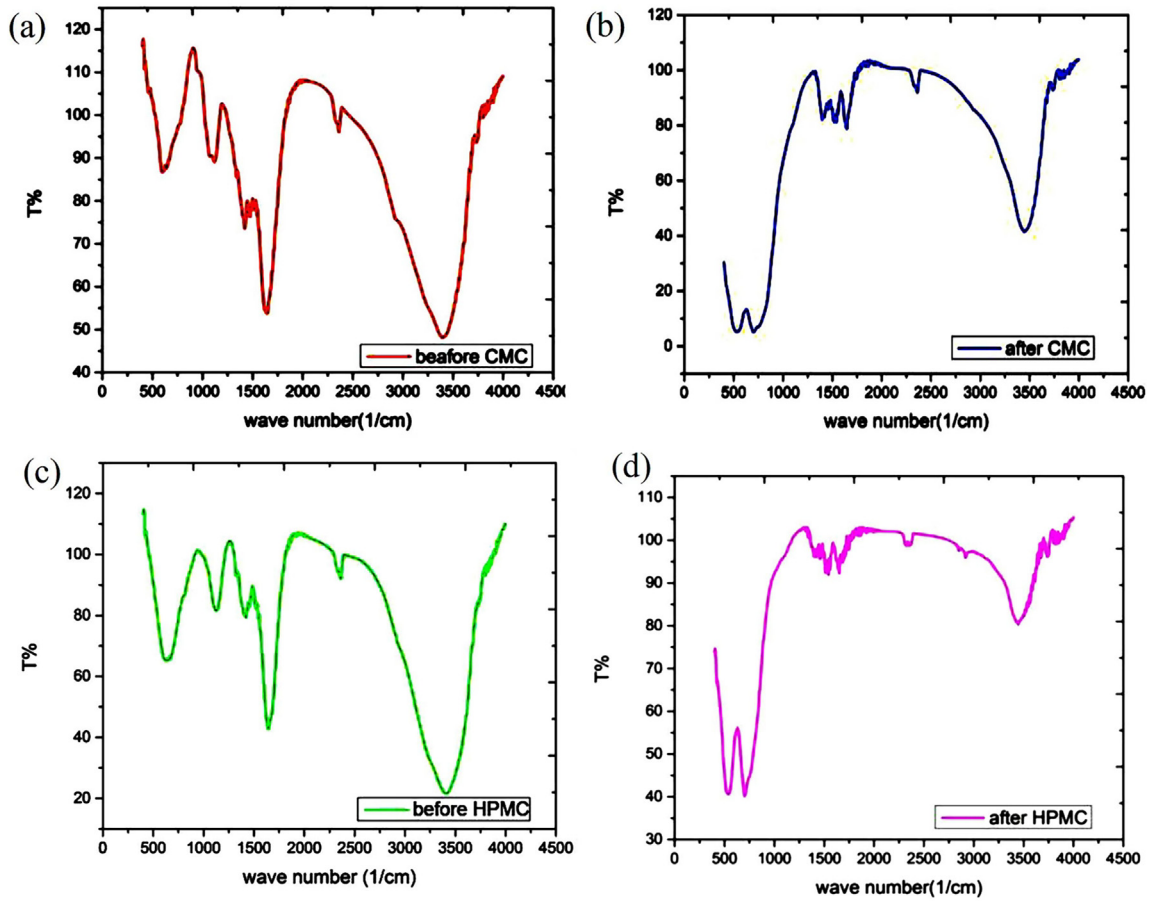

Fig. 3. FTIR spectra of magnesium aluminate with adding carboxymethyl cellulose (a) before the calcination step (b) after the calcination process. (c, d) FTIR test upon adding HPMC agent (c) before calcination (d) after calcination.

2.4. Sintering of samples via spark plasma sintering (SPS) method

For the sintering process, an SPS device (SPS 60–10, MUT University, Iran) was used. First, 1.5 g of magnesium aluminate nanopowder and 200 ppm of yttrium chloride sintering aid were dispersed in 30 ml water. The mixture of spinel nanopowder and sintering aid was dried at 50 °C for 24 h. The final powder was calcined at 800 °C for 1 h so that the yttrium chloride sintering aid would change into yttrium oxide. Next, the mixed powder with a sintering aid was poured into a graphite mould to obtain a disc with a 20 mm diameter and thickness of 1 mm. In this project, to reduce carbon contamination resulting from graphite mould, a low heating rate was used to achieve the final temperature. Thereafter, the final disc was prepared at 1500 °C and a heating rate of 5 °C under 70 MPa pressure for 15 min. Fig. S1 (see supporting information, Heidari et al., 2021; Heidari et al., 2022) display the utilized SPS cycle. To prepare the disc for the transmission test, the surface of the samples was polished with SiC sandpaper (Smirdex, Greece, grade P510), a number 120, 300, 600, 1000, 2000 and 3000.

2.5. Instruments

Fourier transforms infrared (FT-IR) spectra were captured using a disc made of KBr via a spectrophotometer (PLUS-680, JASCO Co.) within the 400–4000 cm^{-1} range with a resolution of 4 cm^{-1} (Budi et al., 2022; Salahdin et al. 2022; Sivaraman et al., 2022). Raman spectroscopy was done by the Horiba Raman instrument (LAB Ram HR model, made in Japan) under an excitation wavelength of 532 nm (Du et al., 2023) . To detect the formed phases (Bakhshkandi and Ghoranneviss, 2019; Jasim et al., 2022; Liu et al., 2022; Sadeghi et al., 2022; Xin et al., 2022), an X-ray diffraction test (XRD) was used via an X-ray diffractometer (X-Pert-MPD, Phillips Co.). The XRD test was done using monochromatic Cu k_α radiation with the wavelength of 1.5046 Å at a voltage of 40 kV and current of 30 mA. The diffraction was done within 2θ range of 10–80 ° with a step size of 0.05° and time per step of 1 s. For observing the morphology of the sample (Abdulrazzaq, 2023; Chupradit et al., 2021; Ghaffar et al., 2022; Raya et al., 2022; Turki Jalil et al., 2021), Field emission scanning electron microscopy (FE-SEM) images (Dong et al., 2023; Ma et al., 2023; Mo et al., 2022; Sun et al., 2023; Wang et al., 2020) were used by an FEI device equipped with an X-ray energy dispersive spectrophotometer. Particle size distributions were drawn with the Digimizer and Excell software with a measuring size of at least 100 particles. TG/DSC analysis was performed on Netzsch Simultaneous Thermal Analyzer (STA/TGA-DSC) under a nitrogen atmosphere (Wang et al., 2020; Xu et al., 2022) from room temperature to 800 °C.

An ultrasonic device (TOPSONIC, Tehran, Iran) was used with a frequency of 20 kHz and the maximum power level of the device (400 W) for the dispersion of nanoparticles (Al-Obaidi et al., 2018; Kadhum et al., 2021, Seyyedi et al., 2021). For calcining the samples in an air atmosphere, a furnace (NCR-Noberterm) was used. For the sintering process, an SPS device (SPS 60–10, MUT University, Iran) was utilized. Linear transmission within 2.5–10 μm was measured using an IR spectrophotometer (FTIR-8400 S, Shimadzu, Japan), SHIMADZU VIS-NIR Spectrophotometer3100-Japan was employed. Visible transmitance was recored on the Unico S2150 model Ultraviolet-Visible spectrometer (Zhao et al., 2022).

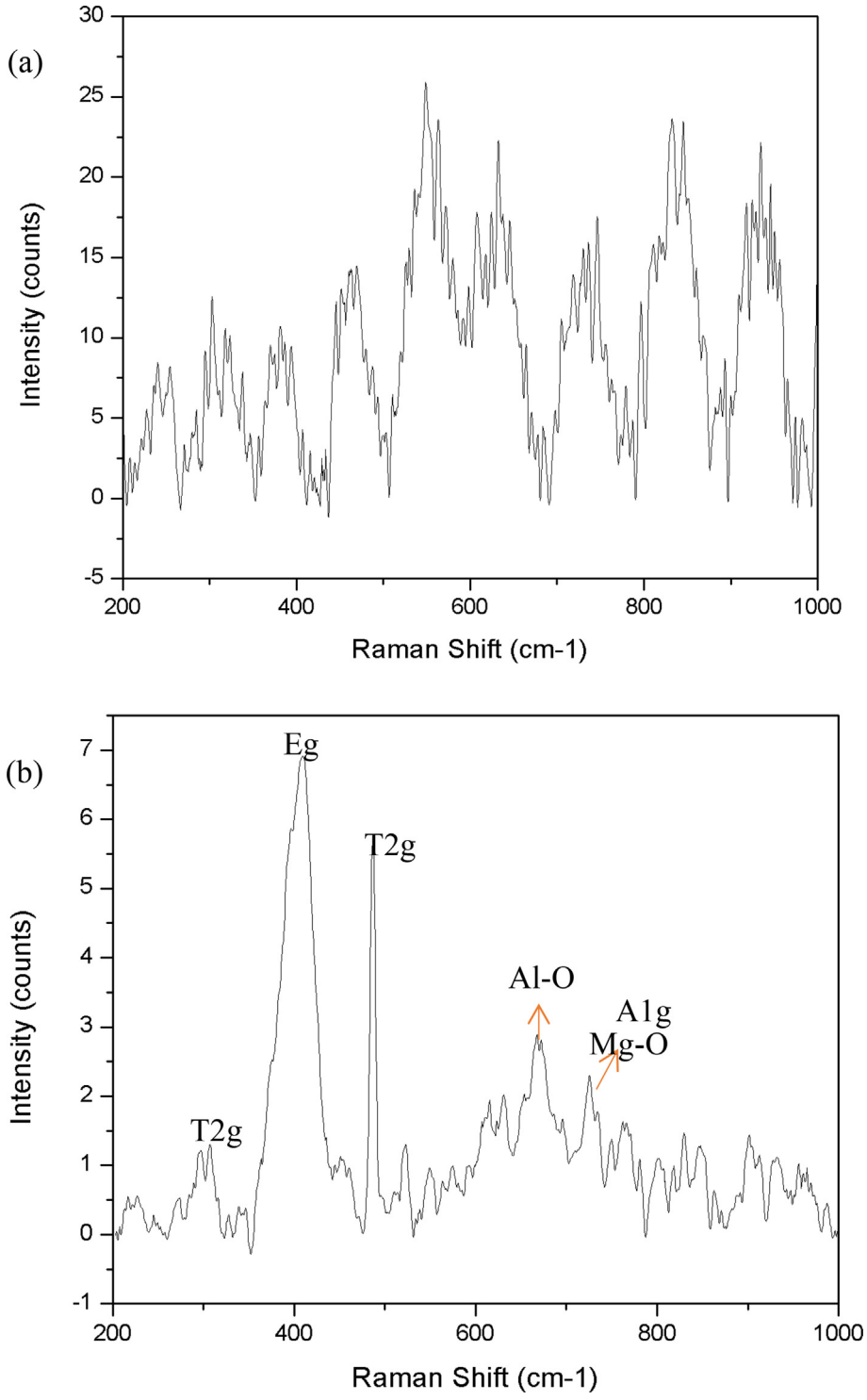

Fig. 4. Raman spectrum of the gel of spinel before (a) and after (b) calcination step.

The density of the sintered samples (P_a) was measured through Archimedes principle based on buoyancy law and via Formula 1 (Sepulveda et al., 2011; Bykov et al., 2019). In this equation, m_1 represents the dry mass, and m_2 denotes the sample mass after immersion in water.

$$P_a = m_1/m_1 - m_2 \quad (1)$$

3. Results and discussion

3.1. XRD patterns of calcined powder

The XRD patterns of magnesium aluminate powder and its comparison with the spinel main card have been shown in Fig. 1. It is seen that upon adding 0.1 g and 0.3 g HPMC to the prepared solution, there are alpha-alumina and magnesium oxide impurities in

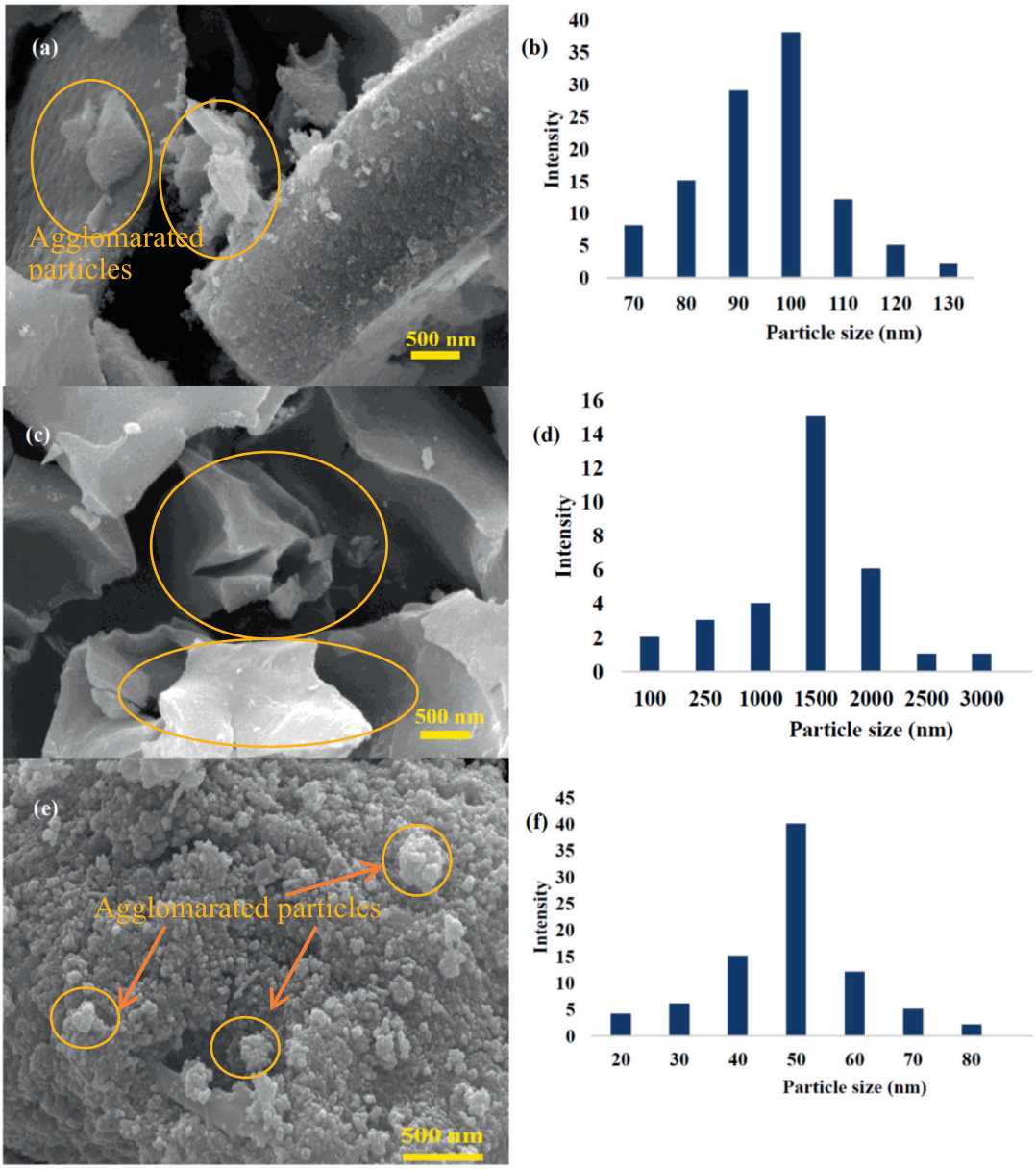

Fig. 5. FESEM images and histogram of magnesium aluminate powder synthesized with (a,b) 0.1 g (c,d) 0.3 g. (e, f) 1 g of CMC by a modified sol–gel method.

addition to the magnesium aluminate phase. Upon adding 0.1–1 g of carboxymethyl cellulose to Mg^{2+}-Al^{3+}-citric acid solution, magnesium aluminate has been achieved completely, and its diffraction card matches the main diffraction card of spinel with the JCPDS number of 01–084-0377. Thus, the use of CMC has been effective in magnesium aluminate synthesis, causing its formation, where different amounts of it have fulfilled this objective. Meanwhile, 1 g of it matches the diffraction pattern of this material.

Also, the diffractions located at 2θ of 31, 36, 44, 59, and 66 are related to (220), (311), (400), (511), and (440) planes, respectively. The wideness of the diffractions results from the fineness of the crystallite size.

Fig. S2 (see supporting information) indicates the XRD pattern of the sample synthesized through the conventional Pechini method calcined at 800 °C. It is observed that with using this precursor, magnesium aluminate has formed as a single phase, matching the standard card No. 01–074-1133, which is related to the cubic crystal with lattice parameters of a = b = c = 0.80850 nm. The reflections at 2θ 18.9, 31.2, 36.8, 44.80, 55.6, 59.3, 65.2, 68.6, 74.10, and 77.3° are related to diffractions of (111), (220), (311), (400), (422), (511), (440), (531), (620), and (533) planes, respectively, indicating magnesium aluminate spinel phase.

3.2. TG/DSC analysis

Fig. 2 shows TGDSC analysis of spinel gel obtained from CMC and HPMC precursor. In both graphs, peaks located at ~ 96–111 °C are related to the removal of water as an endothermic reaction (In DSC curve). Exothermic peaks located at 440 °C and ~ 477–597 °C are related to the burning of citric acid and cellulose derivatives, respectively. As can be seen in the DSC graph, the amount of heat obtained from CMC gel is twice that of HPMC gel (0.6 vs. 1.5 mW/mg). This confirms the X-ray results, which suggest that in the presence of CMC, the spinel network is more fully formed due to the higher heat release of CMC/citric acid gel. According to the TGA curve, up to a temperature of 800 °C, 70% of organic

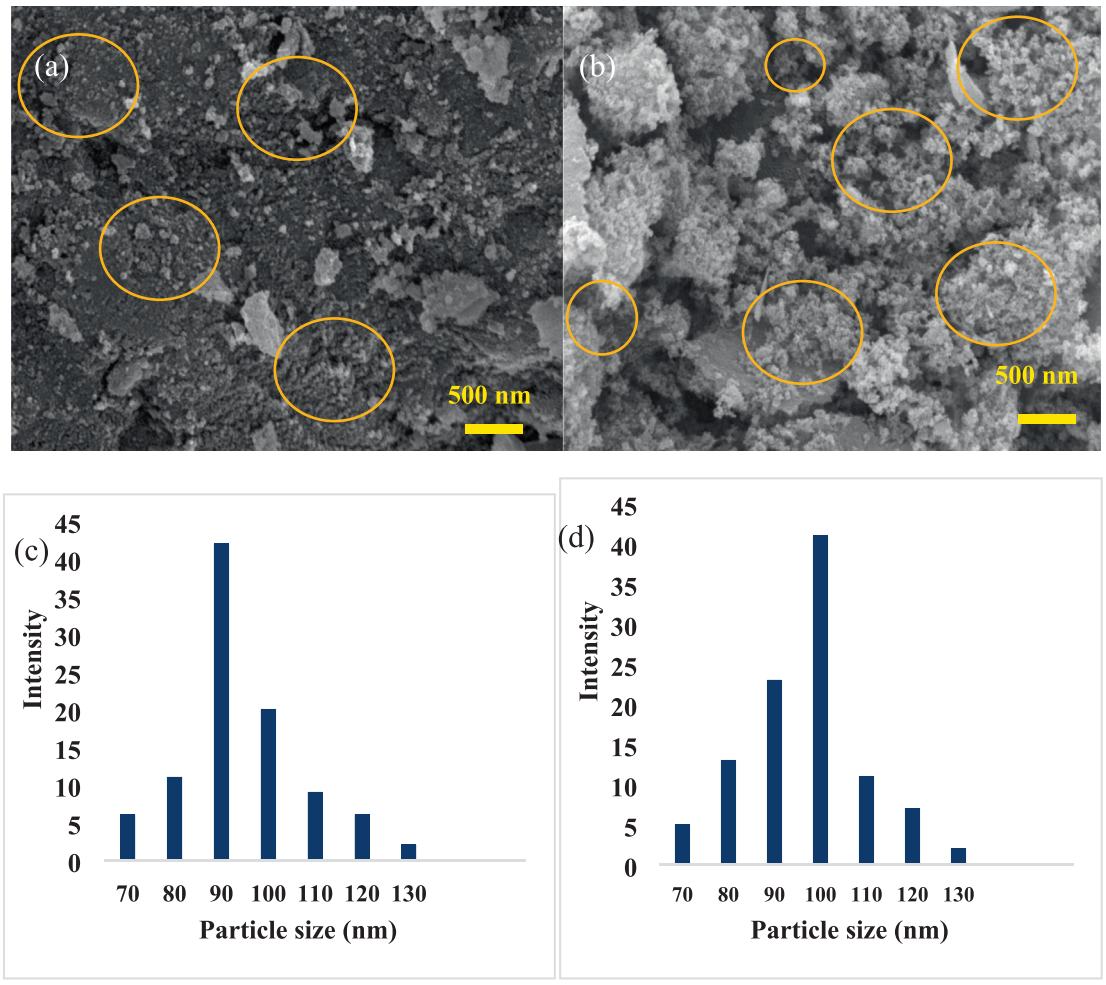

Fig. 6. (a,b) FESEM images and Histogram (c,d) of spinel nanoparticles with (a,c) 0.1 g of HPMC (b,d) 0.3 g of HPMC agent.

matter and adsorbed water are separated from CMC gel and 60% from HPMC gel, which also confirms the better effect of CMC in separating organic matter from the sample. The other point from Fig. 3 is that the weigth loss in the presence of CMC agent (Fig. 3a) occured in 3 steps (before 200 °C, 200-450 °C and 500-800 °C), but in the presence of HPMC, the weigth loss performed on two seps (100-200 °C and 300-800 °C).

3.3. FTIR and Raman spectroscopy

According to Fig. 3, the functional groups related to citric acid and carboxymethyl cellulose can be detected in the precursor of samples (gel) before the calcination stage. After the calcination operations in both cases with carboxymethyl cellulose and hydroxy methyl cellulose, the bands related to the functional groups diminished considerably. At the wavenumber 3400 cm^{-1}, the band is related to the –OH functional group and at the wavenumber of 1600–1700 cm^{-1} double-branched band is seen, indicating the COOH functional group of citric acid. Also, the wavenumber of 2900 cm^{-1} and 1400–1500 cm^{-1} is related to the aliphatic $-CH_2$ vibration (Bokov et al., 2021; Chupradit and Delir Kheirollahi Nezhad, 2022; Jasim et al., 2022; Kadhim et al., 2022; Ngafwan et al., 2021; Raya et al., 2022; Sivaraman et al., 2022; Suanto et al., 2022; Zhao et al., 2022) and the bending vibration of adsorbed water, respectively. In both samples, after the calcination, the intensity of organic bands had relatively diminished.

Fig. 4 shows the Raman spectrum of the gel of spinel before and after the calcination step. According to Fig. 4, the number of Raman modes after calcination is much less, which indicates the improvement of the crystalline order of the spinel network after the calcination step. Spinel's index peaks at frequencies 307, 409, 486, 667, and 762 cm^{-1} correspond to T2g, Eg, T2g, T2g, and A1g vibration modes, respectively. The peaks located in wave numbers 725 and 762 cm^{-1} are related to the disordered breathing stretching vibrations of the Al-O bond and the ordered Mg-O in the AlO_4 and MgO_4 tetrahedral sites, respectively. In a perfect spinel lattice, only the second-ordered vibration is observed (Dwibedi, 2015, Slotznick 2008).

3.4. SEM images of magnesium aluminate powders

Fig. 5 shows the SEM images of the spinel powder synthesized via the modified Pechini method by adding a CMC chelating agent. The morphology of this powder with 0.1 and 0.3 g CMC is irregular with agglomerated particles with the size of 500 nm –1 μm.

According to the observations, upon adding 1 g of CMC, the morphology of the powder has been finer, with an average particle size of 50 nm. Furthermore, the size of agglomerated particles was reduced from 1 μm (0.3 g CMC, Fig. 3c) to 250–300 nm (see orange ring in Fig. 5).

Fig. 6 displays the SEM images of magnesium aluminate powder synthesized with an HPMC chelating agent. Based on these images, the use of an HPMC additive has caused the agglomeration of particles with an agglomerated particle size of 500 nm-1 μm (see orange ring in the SEM images). Thus, the powder quality has

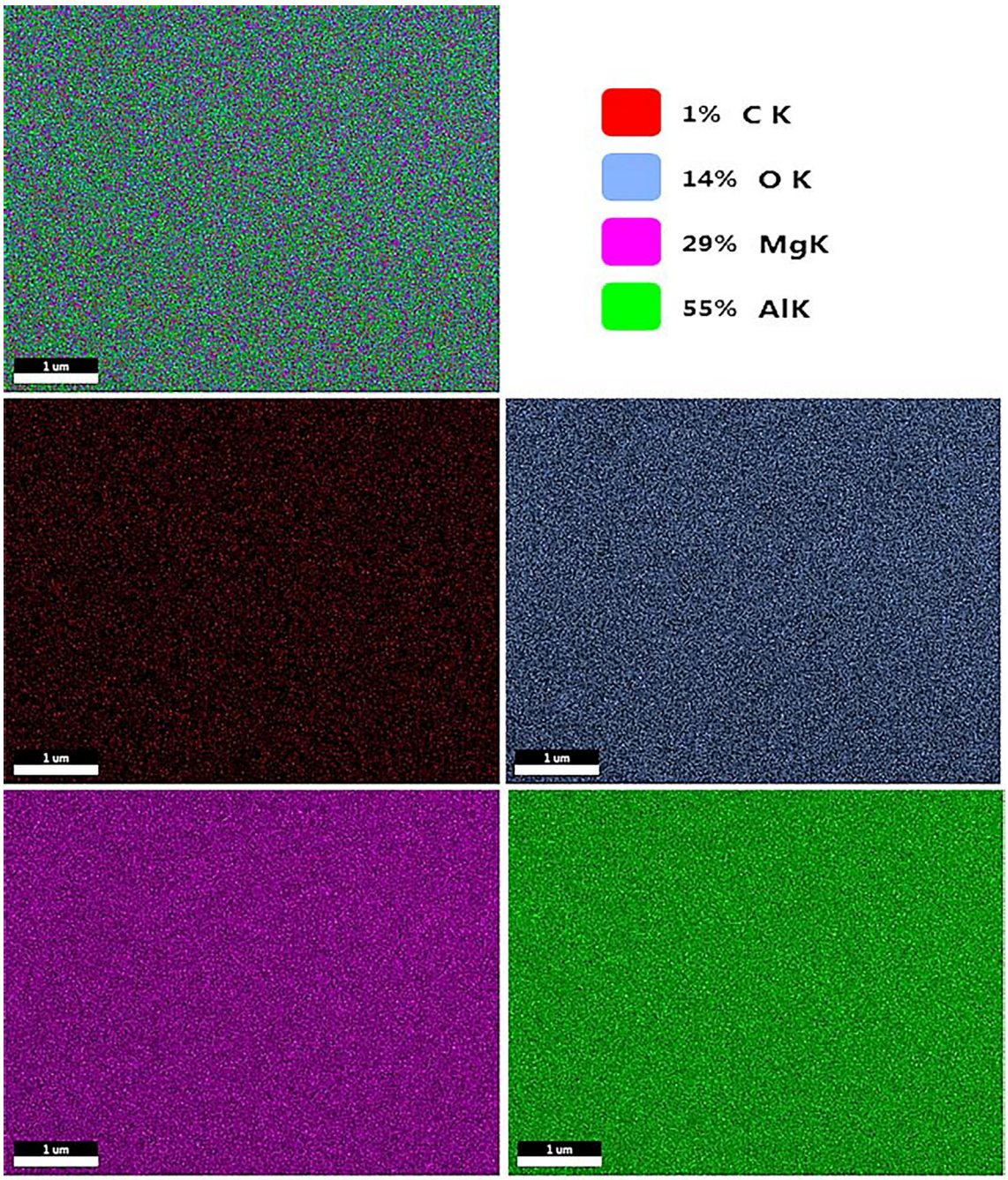

Fig. 7. EDS elemental mapping of the sample synthesized via the Pechini sol–gel method modified with 1 g of CMC agent.

diminished compared to 1 g of CMC as less agglomeration occurred in it.

In the Pechini method, Al and Mg cations form complexes through chelating agents (citric acid molecules, (Dimesso, 2016)). Then, the polyester network is formed through ethylene glycol as the gel-forming agent (Fig. S3, see supporting information). In the polyester network, hydrogen attraction occurs between the oxygen of carboxylic acid groups and hydrogen of the –OH functional group in the chain. This attraction is so strong that the polyester supramolecules chains (Liu et al., 2023; Sun et al., 2023) approach each other, where the final spinel nanoparticles obtained from polyester gel calcination have much agglomeration (Medvedev et al., 2022; Mamonova et al., 2017).

Upon substituting ethylene glycol with 1 g CMC, the formed hydrogen bonds of the polyester gel may diminish, whereby the polyester chains move slightly apart from each other. The complex formation between metal ions and CMC molecules (Fig. S3) helps polyester chains reduce the agglomeration degree and particle size of spinel nanoparticles through the modified Pechini method (particle size of 50 nm and agglomerated particle size of 20–300 nm). However, with using a low amount of CMC (0.1 g and 0.3 g CMC), the number of CMC-M^{n+} complexes was low, and the extent of hydrogen bonds was high in the polyester chain. Thus, particle size, in this case, was 500 nm-1000 nm.

Fig. S4 (see supporting information) reveals the FESEM image of the sample synthesized via the conventional Pechini method. It is seen that at 800 °C, the morphology is spherical, and the size of the nanoparticles is between 100 and 400 nm. The X-ray map of this sample (Fig. S5, see supporting information) shows uniform distribution of O, Al, and Mg elements in the sample.

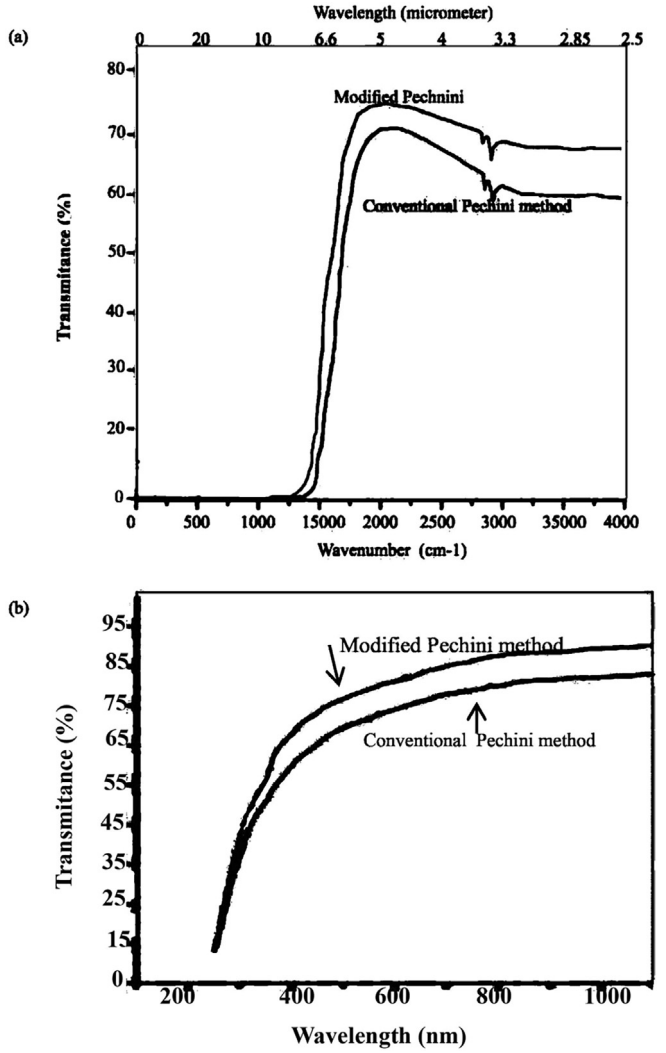

Fig. 8. (a) IR transmission curve and (b) UV–VIS transmission curve of the sample sintered through SPS at 1500 °C from modified and conventional Pechini powder.

Fig. 7 exhibits an X-ray elemental map of the sample synthesized via the Pechini method modified with 1 g of CMC. This image shows the presence of aluminium, magnesium, and oxygen elements in the spinel nanoparticles. Furthermore, the uniform distribution of each element in the EDS mapping test confirms the homogenous formation of magnesium aluminate spinel in the samples synthesized via the modified Pechini method.

Fig. S5 (see supporting information) reveals the EDS mapping of the sample synthesized through the conventional Pechini method. In this image, again, large aggregated particles, as well as the distribution of aluminium, magnesium, and oxygen elements, can be observed.

3.5. Sintering of the sample synthesized via the SPS

3.5.1. Phase examination of the spinel ceramics body

Fig. S6 (see supporting information) depicts the XRD pattern of the sample sintered through the SPS method. As seen, there is great correspondence with the reference pattern of spinel magnesium aluminate. It can also be found that during the sintering, phase transformation has not occurred in the material, and the structure is still cubic. The lattice parameters based on the matched standard card of this sample have been a = b = c = 0.8068 nm. The peaks at 2θ of 18.9, 31.2, 36.8, 44.80, 55.6, 59.3, 65.2, 68.6, 74.10, and 77.3° are related to diffraction/reflection of (111), (220), (311), (400), (422), (511), (440), (531), (620), and (533) planes respectively, indicating magnesium aluminate spinel phase.

Fig. S6 and Fig. S7 (see supporting information) illustrate the XRD pattern of the disc-shaped sample of magnesium aluminate spinel prepared via the SPS method through the powder made by the conventional Pechini method calcined at 800 °C. According to the figure, the magnesium aluminate spinel has formed in a full single phase and matches the standard card 01–075-1795.

3.5.2. Optical transmittance, microstructure and density of spinel ceramics body

Fig. 8a exhibits the IR transmission curve of the sample SPSed at 1500 °C. According to this figure, there is an absorption peak resulting from the presence of CH_2 organic groups at a wavelength of 3.4 μm. Fig. 8b depicts the visible light transmission curve within 400–800 nm of the spinel sample sintered at 1500 °C. Based on this figure, the SPSed sample prepared with the modified sol-gel method at 550 nm has a transmittance of 75% and has approached spinel theoretical transmission, being 87%. The maximum IR transmission of the sample prepared through sintering of the sample prepared with the modified Pechini method was 74 % at a wavelength of 5 μm (2000 cm^{-1}). At this wavelength, the sample prepared through the conventional Pechini method showed 70% transmission with a sample thickness of 1 mm.

Fig. 9 shows the cross-sectional morphology of the spinel disc chemically –etched (hot concentered H_2SO_4 solution for 1 min). Fig. 9(a,b) reveals porosity in the disc sintered from the spinel nanopowder produced via the conventional Pechini method (98.82% of theoretical density). Fig. 9(c,d) indicates a lack of porosity in the sample sintered from modified Pechini powder, confirming densification with minimum sample porosity (Heidari et al. 2021). The Archimedes density of this sample has also been 99.98% of the theoretical density.

Fig. 9e reveals the EDS of the sample sintered from the modified Pechini method. According to this analysis, magnesium, aluminium, and oxygen elements related to the magnesium aluminate phase, as well as the yttrium element related to the yttria sintering aid, are present in the sintered sample. The presence of slight amounts of carbon in the EDS analysis is probably related to the diffusion of SPS mould graphite to the spinel along the sintering process.

According to actual image of sintered body, there is some darkness at the edge of the discs, possibly associated with the diffusion of graphite from the SPS mould into the spinel sample. The presence of CH_2 in Fig. 8 at wavnumber of 2900 cm^{-1} was also confirmed this fact (Chen et al., 2021, 2023; Huang et al., 2023; Kuang et al., 2018; Li et al., 2022; Liu et al., 2023; Lu et al., 2023; Sha et al., 2023; Zhang et al., 2016; Zhao et al., 2022).

Theoretically, magnesium aluminate spinel has 87% transmission within the IR average range (Senina et al., 2019; Izadbakhsh et al., 2021; Bykov et al., 2019; Azizi-Malekabadi et al., 2020; Baruah et al., 2023). The transmission obtained in this project has been lower than the theoretical density. The reduction of the transmission percentage of the final piece can be attributed to the presence of pores. To achieve greater transparency, the use of high-quality initial powder and less agglomeration of spinel nanopowder is required. The pores cause light scattering and, ultimately, translucence of the final piece. With the removal or reduction of each of the mentioned points, a higher transmission percentage can be achieved.

4. Conclusion

The manuscript proposes the synthesis of homogeneous magnesium aluminate spinel ceramics using cellulose derivatives and

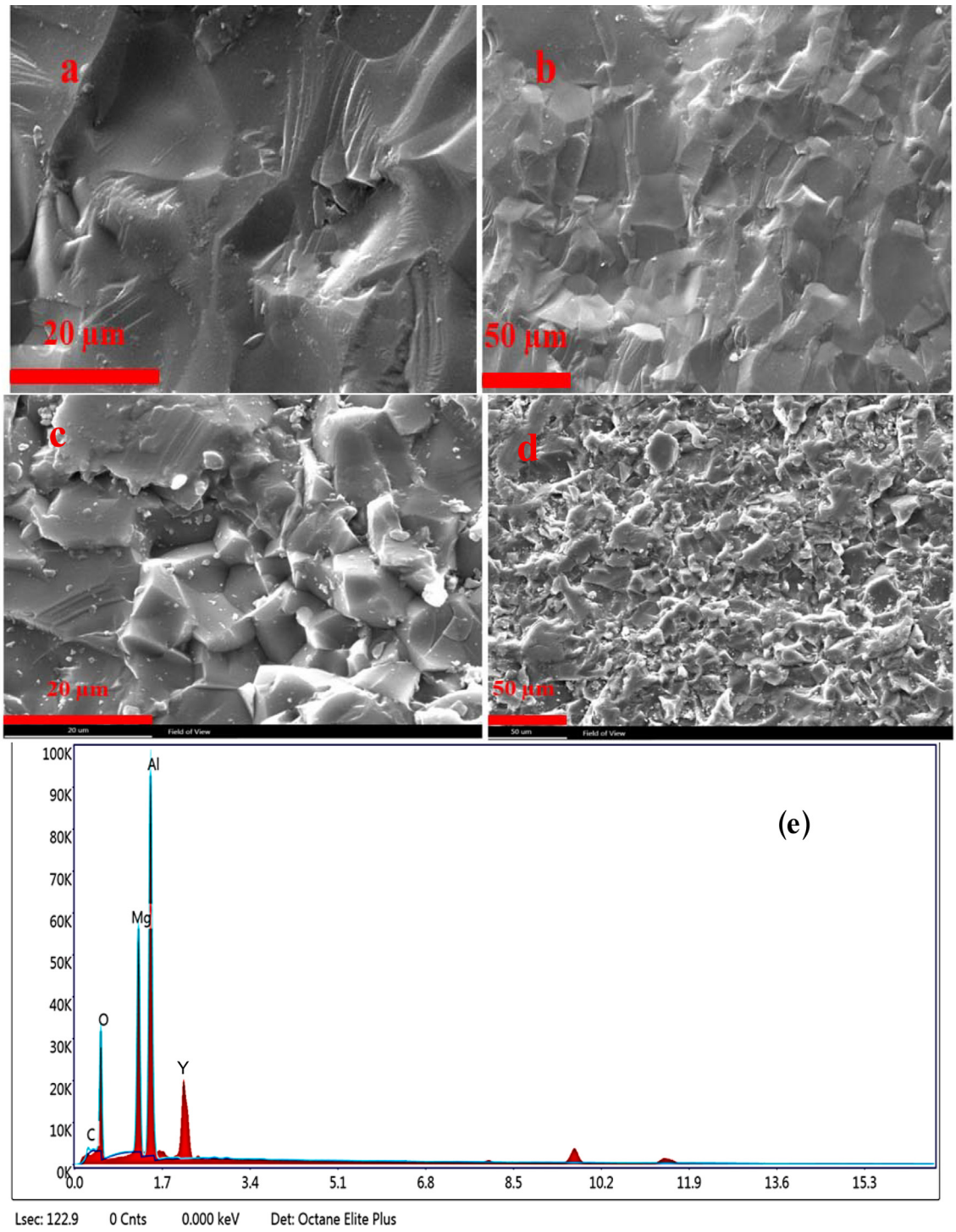

Fig. 9. FESEM images of the fractured cross-section of bulk sample originated from (a,b) modified Pechini methods and (c,d) conventional Pechini methods, (e) EDS analysis of the sintered sample from the modified Pechini method.

the sol–gel method to obtain a better ceramic material without particle agglomeration. The results indicated that the Pechini sol–gel method modified with 1 g of CMC offered a smaller particle size (50 nm) as well as less agglomeration compared to the conventional Pechini method (particle size of 100–400 nm).

In synthesizing the magnesium aluminate nanoparticles, the addition of carboxymethyl cellulose was far more effective than adding hydroxy methyl cellulose, and the XRD pattern of the samples synthesized with CMC fully matched that of magnesium aluminate. The 1 g of CMC had a greater effect on the synthesis of magnesium aluminate compared to 0.1 and 0.3 g of it.

The calcination process on the synthesized powders led to the removal of functional groups and reduction of the intensity of FTIR bands related to the functional groups in the sol–gel process.

The disc created using the powder prepared through the conventional Pechini method had 70% transmission within the 5 µm region, as well as an apparent density of 99.38%. However, the linear transmission of the disc prepared through the modified Pechini

method was 75% in the 5 μm range. The density of this sample was obtained at 99.98%.

CRediT authorship contribution statement

Fuqiu Ye: Conceptualization, Funding acquisition, Methodology, Project administration, Validation. **M. Sadeghi:** Conceptualization, Writing - review & editing. **M.R. Loghman Estarki:** Conceptualization, Funding acquisition, Methodology, Project administration, Formal analysis, Supervision.

Declaration of Competing Interest

The authors declare that they have no known competing financial interests or personal relationships that could have appeared to influence the work reported in this paper.

Acknowledgement

Authors should tahnk from S. Haghpanah (from MUT university) and N. Heidari (from IUT university) for performing experimental synthesizing and sintering of spinel nanopowders.

Appendix A. Supplementary material

Supplementary data to this article can be found online at https://doi.org/10.1016/j.arabjc.2023.105198.

References

Abdulrazzaq, M., 2023. Surface cracks growth for superalloy in a round bar under different loading. Metall. Mater. Eng. 29 (1), 83–89.
Akhlaghi, N., Najafpour-Darzi, G., 2022. Preparation of immobilized lipase on Co^{2+}-chelated carboxymethyl cellulose based $MnFe_2O_4$ magnetic nanocomposite particles. Mol. Catal. 519, 112118.
Al-Obaidi, Z.M.J., Mohammed, H.R., Ebrahim Al Ani, A.A., 2018. The employment of standard addition method for the UV spectrophotometric assay of diclofenac alkaline salts in variant pharmaceutical dosage forms. J. Global Pharma Technol. 10 (11), 377–382.
Azizi-Malekabadi, M., Sarraf-Mamoory, R., 2020. Devising a novel method of producing high transparent magnesium aluminate spinel ($MgAl_2O_4$) ceramics body using synthesized LiF nanopowder and spark plasma sintering. Mater. Chem. Phys. 250, 123035.
Bakhshkandi, R., Ghoranneviss, M., 2019. Investigating the synthesis and growth of titanium dioxide nanoparticles on a cobalt catalyst. J. Res. Sci. Eng. Technol. 7 (4), 1–3.
Baruah, B., Sarkar, R., 2023. Effect of Y_2O_3 content on densification, microstructure and mechanical properties of reaction sintered magnesium aluminate spinel. Ceram. Int. 49 (1), 755–765.
Bokov, D., Turki Jalil, A., Chupradit, S., Suksatan, W., Javed Ansari, M., Shewael, I.H., Kianfar, E., 2021. Nanomaterial by sol-gel method: synthesis and application. Adv. Mater. Sci. Eng. 2021, 1–21.
Budi, H.S., Davidyants, A., Rudiansyah, M., Ansari, M.J., Suksatan, W., Sultan, M.Q., Kazemnejadi, M., 2022. Alendronate reinforced polycaprolactone-gelatin-graphene oxide: A promising nanofibrous scaffolds with controlled drug release. Mater. Today Commun. 32, 104108.
Bykov, Y.V., Egorov, S.V., Eremeev, A.G., Kholoptsev, V.V., Plotnikov, I.V., Rybakov, K. I., Belyaev, A.V., 2019. Ultra-rapid microwave sintering of pure and Y_2O_3-doped $MgAl_2O_4$. J. Am. Ceram. Soc. 102 (2), 559–568.
Chen, L., Zhao, Y., Jing, J., Hou, H., 2023. Microstructural evolution in graphene nanoplatelets reinforced magnesium matrix composites fabricated through thixomolding process. J. Alloys Compds. 940, 168824.
Chen, L., Zhao, Y., Li, M., Li, L., Hou, L., Hou, H., 2021. Reinforced AZ91D magnesium alloy with thixomolding process facilitated dispersion of graphene nanoplatelets and enhanced interfacial interactions. Mat. Sci. Eng. A 804, 140793.
Chupradit, S., Delir Kheirollahi Nezhad, P., 2022. Ir-decorated gallium nitride nanotubes as a chemical sensor for recognition of mesalamine drug: a DFT study. Molecular Simulation 48 (5), 438–447.
Chupradit, S., Jalil, A.T., Enina, Y., Neganov, D.A., Alhassan, M.S., Aravindhan, S., Davarpanah, A., 2021. Use of organic and copper-based nanoparticles on the turbulator installment in a shell tube heat exchanger: a CFD-based simulation approach by using nanofluids. J. Nanomater. 2021, 1–7.
Dimesso, L., 2016. Pechini processes: an alternate approach of the sol–gel method, preparation, properties, and applications. Handbk. Sol-Gel Sci. Technol. 2, 1–22.
Dong, S., Zhang, H., Yuan, D., 2023. Supramolecular Nonwoven Materials via Thermally Induced Precursor Crystallization of Nanocrystalline Fibers/Belts for Recyclable Air Filters. ACS Appl. Nano Mat. 6 (11), 9548–9557.
Du, S., Xie, H., Yin, J., Fang, T., Zhang, S., Sun, Y., Zheng, R., 2023. Competition Pathways of Energy Relaxation of Hot Electrons through Coupling with Optical, Surface, and Acoustic Phonons. J. Phys. Chem.C 127 (4), 1929–1936.
Durai, L., Badhulika, S., 2022. Spinel structured $MgAl_2O_4$ nanoparticles as a low-cost and stable SERS substrate for rapid simultaneous detection of neurological drugs in biofluids. Ceram. Int. 48 (13), 18667–18675.
Dwibedi, D., Avdeev, M., Barpanda, P., 2015. Role of fuel on cation disorder in magnesium aluminate ($MgAl_2O_4$) spinel prepared by combustion synthesis. J. Am. Ceram. Soc. 98 (9), 2908–2913.
Ghaffar, S., Naqvi, M.A., Fayyaz, A., Abid, M.K., Khayitov, K.N., Jalil, A.T., Nouri, M., 2022. What is the influence of grape products on liver enzymes? A systematic review and meta-analysis of randomized controlled trials. Complement. Ther. Med. 69, 102845.
Gogoi, B., Das, U., 2022. Structural, Magnetic and Thermal Characteristic Analysis of Synthesized Magnetite Spinel Ferrite. Nanoparticles 1-20 https://doi.org/10.21203/rs.3.rs-2034802/v1.
Hasanpour, F., Taei, M., Banitaba, S.H., Heidari, M., 2017. Template synthesis of maghemite nanoparticle in carboxymethyl cellulose and its application for electrochemical cabergoline sensing. Mater. Sci. Eng. C 76, 88–93.
Heidari, N., Davar, F., Alhaji, A., 2022. In situ formation of transparent spinel with the spark plasma sintering of magnesia-alumina nanocomposite granules without the help of sintering aid. Ceram. Int. 48 (2), 1633–1641.
Heidari, N., Davar, F.(supervisor), Loghman Estarki, idari et al. 2021.. PhD thesis: Synthesis of MgO-Al_2O_3 nanocomposite and their use for the production of transparent spinel body with the spark plasma sintering method. M.R.(advisor Isfahan University of Technology, Iran, pp. 1–100.
Huang, G., Kong, Q., Yao, W., Wang, Q., 2023. High Proportion of Active Nitrogen-Doped Hard Carbon Based on Mannich Reaction as Anode Material for High-Performance Sodium-Ion Batteries. ChemSusChem 16, (7) e202202070.
Izadbakhsh, H., Sheikh, H., Sharifi, E.M., Alhaji, A., Loghman-Estarki, M.R., Ramazani, M., 2021. Development of mechanical and visible transparency properties of spark plasma sintered spinel fabricated by powder injection molding of $MgAl_2O_4$ nanoparticles. Ceram. Int. 47 (21), 29707–29711.
Jasim, S.A., Hadi, J.M., Opulencia, M.J.C., Karim, Y.S., Mahdi, A.B., Kadhim, M.M., Falih, K.T., 2022. MXene/metal and polymer nanocomposites: preparation, properties, and applications. J. Alloy. Compd. 917, 165404.
Jasim, S.A., Hachem, K., Abed Hussein, S., Turki Jalil, A., Hameed, N.M., Dehno Khalaji, A., 2022. New chitosan modified with epichlohydrin and bidentate Schiff base applied to removal of Pb^{2+} and Cd^{2+} ions. J. Chin. Chem. Soc. 69 (7), 1051–1059.
Kadhim, M.M., Sead, F.F., Jalil, A.T., Taban, T.Z., Rheima, A.M., Almashhadani, H.A., Hamel, S., 2022. Al-, Ga-, and In-decorated BP nanotubes as chemical sensors for 2-chloroethanol. Monatshefte Chem.-Chem. Monthly 153 (7–8), 589–596.
Kadhum, W.R., Al-Zuhairy, S.A., Mohamed, M.B., Abdulrahman, A.Y., Kadhim, M.M., Alsadoon, Z., Teoh, T.C., 2021. A nanotechnological approach for enhancing the topical drug delivery by newly developed liquid crystal formulations. IJDDT 11 (3), 716–721.
Kuang, W., Wang, H., Li, X., Zhang, J., Zhou, Q., Zhao, Y., 2018. Application of the thermodynamic extremal principle to diffusion-controlled phase transformations in Fe-C-X alloys: Modeling and applications. Acta Mater. 159, 16–30.
Li, M., Guo, Q., Chen, L., Li, L., Hou, H., Zhao, Y., 2022. Microstructure and properties of graphene nanoplatelets reinforced AZ91D matrix composites prepared by electromagnetic stirring casting. J. Mater. Res. Technol. 21, 4138–4150.
Liu, Y., Fan, B., Xu, B., Yang, B., 2023. Ambient-stable polyethyleneimine functionalized $Ti_3C_2T_x$ nanohybrid corrosion inhibitor for copper in alkaline electrolyte. Mater. Let. 337, 133979.
Liu, Z., Fan, B., Zhao, J., Yang, B., Zheng, X., 2023. Benzothiazole derivatives-based supramolecular assemblies as efficient corrosion inhibitors for copper in artificial seawater: Formation, interfacial release and protective mechanisms. Corr. Sci. 212, 110957.
Liu, B., Khalid, I., Patra, I., Kuzichkin, O.R., Sivaraman, R., Jalil, A.T., Hekmatifar, M., 2022. The effect of hydrophilic and hydrophobic surfaces on the thermal and atomic behavior of ammonia/copper nanofluid using molecular dynamics simulation. J. Mol. Liq. 364, 119925.
Lu, J., Fan, X., Hu, J., Li, J., Rong, J., Wang, W.. . .Chen, Y., 2023. Construction and function of robust and moist bilayer chitosan-based hydrogel wound dressing. Mater. Des. 226, 111604.
Ma, G., He, P., Wang, H., Tian, H., Zhou, L., Yong, Q.. . .He, D., 2023. Promoting bonding strength between internal Al-Si based gradient coating and aluminum alloy cylinder bore by forming homo-epitaxial growth interface. Mater.Des. 227, 111764.
Mamonova, D.V., Kolesnikov, I.E., Manshina, A.A., Mikhailov, M.D., Smirnov, V.M., 2017. Modified Pechini method for the synthesis of weakly-agglomerated nanocrystalline yttrium aluminum garnet (YAG) powders. Mater. Chem. Phys. 189, 245–251.
Medvedev, V.A., Shubina, I.M., Kolesnikov, I.E., Lähderanta, E., Mikhailov, M.D., Manshina, A.A., Mamonova, D.V., 2022. Synthesis of weakly-agglomerated luminescent $CaWO_4$: Nd^{3+} particles by modified Pechini method. Ceram. Int. 48 (4), 5100–5106.
Mo, X., Liu, X., Chen, J., Zhu, S., Xu, W., Tan, K., Liu, W., 2022. Separation of lattice-incorporated Cr(vi) from calcium carbonate by converting microcrystals into

nanocrystals via the carbonation pathway based on the density functional theory study of incorporation energy. Environ. Sci.: Nano 9 (5), 1617–1626.
Nassar, M.Y., Ahmed, I.S., Samir, I., 2014. A novel synthetic route for magnesium aluminate ($MgAl_2O_4$) nanoparticles using sol–gel auto combustion method and their photocatalytic properties. Spectrochim. Acta A Mol. Biomol. Spectrosc. 131, 329–334.
Ngafwan, N., Rasyid, H., Abood, E.S., Abdelbasset, W.K., Al-Shawi, S.G., Bokov, D., Jalil, A.T., 2021. Study on novel fluorescent carbon nanomaterials in food analysis. Food Sci. Technol. 42, e37821.
Raya, I., Chupradit, S., Kadhim, M.M., Mahmoud, M.Z., Jalil, A.T., Surendar, A., Bochvar, A.N., 2022. Role of compositional changes on thermal, magnetic, and mechanical properties of Fe-PC-based amorphous alloys. Chin. Phys. B 31, (1) 016401.
Raya, I., Danshina, S., Jalil, A.T., Suksatan, W., Mahmoud, M.Z., Roomi, A.B., Kazemnejadi, M., 2022. Catalytic filtration: efficient CC cross-coupling using Pd (II)-salen complex-embedded cellulose filter paper as a portable catalyst. RSC Adv. 12 (31), 20156–20173.
Rothman, A., Kalabukhov, S., Sverdlov, N., Dariel, M.P., Frage, N., 2014. The effect of grain size on the mechanical and optical properties of spark plasma sintering-processed magnesium aluminate spinel M g A l2 O 4. Int. J. Appl. Ceram. Technol. 11 (1), 146–153.
Sadeghi, M., Yousefi Siavoshani, A., Bazargani, M., Jalil, A.T., Ramezani, M., Poor Heravi, M.R., 2022. Dichlorosilane adsorption on the Al, Ga, and Zn-doped fullerenes. Monatshefte Chem.-Chem. Monthly 153 (5–6), 427–434.
Salahdin, O.D., Sayadi, H., Solanki, R., Parra, R.M.R., Al-Thamir, M., Jalil, A.T., Kianfar, E., 2022. Graphene and carbon structures and nanomaterials for energy storage. Appl. Phys. A 128 (8), 703.
Sanjabi, S., Obeydavi, A., 2015. Synthesis and characterization of nanocrystalline $MgAl_2O_4$ spinel via modified sol–gel method. J. Alloy. Compds. 645, 535–540.
Senina, M.O., Lemeshev, D.O., Vershinin, D.I., Boiko, A.V., Pedchenko, M.S., 2019. Effect of B_2 O_3 concentration on the properties of transparent magnesium aluminate spinel ceramics. Inorg. Mater. 55, 846–850.
Sepulveda, J. L., Loutfy, R. O., Chang, S., & Ibrahim, S. (2011, May). High-performance spinel ceramics for IR windows and domes. In Window and dome technologies and materials XII (Vol. 8016, pp. 32-43). SPIE.
Seyyedi, M., Molajou, A., 2021. Nanohydroxyapatite loaded-acrylated polyurethane nanofibrous scaffolds for controlled release of paclitaxel anticancer drug. J. Res. Sci. Eng. Technol. 9 (01), 50–61.
Sha, L., Sui, B., Wang, P., Gong, Z., Zhang, Y., Wu, Y.. . .Shi, F., 2023. Printing 3D mesh-like grooves on zinc surface to enhance the stability of aqueous zinc ion batteries. J. Colloid Interface Sci. 647, 421–428.
Sivaraman, R., Patra, I., Opulencia, M.J.C., Sagban, R., Sharma, H., Jalil, A.T., Ebadi, A. G., 2022. Evaluating the potential of graphene-like boron nitride as a promising cathode for Mg-ion batteries. J. Electroanal. Chem. 917, 116413.
Slotznick, S.P., Shim, S.H., 2008. In situ Raman spectroscopy measurements of $MgAl_2O_4$ spinel up to 1400 C. Am. Miner. 93 (2–3), 470–476.
Suanto, P., Usman, A.P., Saggaff, A., Ismail, M., Khalid, N.H.A., 2022. The characterization of nanocellulose with various durations and NaOH concentration. Int. J. Innov. Res. Scient. Stud. 5 (1), 18–29.
Sun, N., Yao, X., Liu, J., Li, J., Yang, N., Zhao, G.. . .Dai, C., 2023. Breakup and coalescence mechanism of high-stability bubbles reinforced by dispersed particle gel particles in the pore-throat micromodel. Geoenergy Sci. Eng. 223, 211513.
Sun, Q., Zhu, M., Wang, Q., Zhu, C., Yang, J., Li, W., 2023. Design of novel quasi-trivalent dual-main-phase Ce magnets with high performance by manipulating the chemical state of Ce. Acta Mater. 246, 118703.
Sutorik, A.C., Gilde, G., Cooper, C., Wright, J., Hilton, C., 2012. The effect of varied amounts of LiF sintering aid on the transparency of alumina rich spinel ceramic with the composition $MgO_{1.5}$ Al_2O_3. J. Am. Ceram. Soc. 95 (6), 1807–1810.
Turki Jalil, A., Emad Al Qurabiy, H., Hussain Dilfy, S., Oudah Meza, S., Aravindhan, S., M Kadhim, M., & M Aljeboree, A. 2021. CuO/ZrO_2 nanocomposites: facile synthesis, characterization and photocatalytic degradation of tetracycline antibiotic. J. Nanostruct. 11(2), 333-346.
Wang, Z., Chen, C., Liu, H., Hrynshpan, D., Savitskaya, T., Chen, J., Chen, J., 2020. Enhanced denitrification performance of Alcaligenes sp. TB by Pd stimulating to produce membrane adaptation mechanism coupled with nanoscale zero-valent iron. Sci. Total Env. 708, 135063.
Wang, J., Chong, X., Lv, L., Wang, Y., Ji, X., Yun, H., Feng, J., 2023. High-entropy ferroelastic $(10RE_{0.1})TaO_4$ ceramics with oxygen vacancies and improved thermophysical properties. J. Mater. Sci. Technol. 157, 98–106.
Wang, J., Pan, Z., Wang, Y., Wang, L., Su, L., Cuiuri, D., Li, H., 2020. Evolution of crystallographic orientation, precipitation, phase transformation and mechanical properties realized by enhancing deposition current for dual-wire arc additive manufactured Ni-rich NiTi alloy. Addit. Manufact. 34, 101240.
Wen, Y., Liu, X., Chen, X., Jia, Q., Yu, R., Ma, T., 2017. Effect of heat treatment conditions on the growth of $MgAl_2O_4$ nanoparticles obtained by sol-gel method. Ceram. Int. 43 (17), 15246–15253.
Xin, T., Tang, S., Ji, F., Cui, L., He, B., Lin, X., Ferry, M., 2022. Phase transformations in an ultralight BCC Mg alloy during anisothermal ageing. Acta Mater. 239, 118248.
Xu, P., Yuan, Q., Ji, W., Yu, R., Wang, F., Huo, N., 2022. Study on the annealing phase transformation mechanism and electrochemical properties of carbon submicron fibers loaded with cobalt. Mater. Express. 12 (12), 1493–1501.
Zhang, X., Tang, Y., Zhang, F., Lee, C., 2016. A Novel Aluminum-Graphite Dual-Ion Battery. Adv. Energy Mater. 6 (11), 1502588.
Zhang, Y., Wang, S., Liu, B., Hao, Y., 2023. Effect of R_2O_3 (R= Y, La) on the microstructure, optical, and photoluminescent properties of $MgAl_2O_4$: Cr^{3+} transparent ceramics. Opt. Mater. 136, 113454.
Zhao, G., Hooman, M., Yarigarravesh, M., Algarni, M., Opulencia, M.J.C., Alsaikhan, F., Sarjadi, M.S., 2022. Vibration analysis of size dependent micro FML cylindrical shell reinforced by CNTs based on modified couple stress theory. Arab. J. Chem. 15, (10) 104115.
Zhao, Q., Liu, J., Yang, H., Liu, H., Zeng, G., Huang, B.,... Jia, J. 2022. Double U-groove temperature and refractive index photonic crystal fiber sensor based on surface plasmon resonance. Appl. Opt., 61(24), 7225-7230.